

# A New Proposal to Jefferson Lab PAC48

## Measurement of the Two-Photon Exchange contribution to the electron-neutron elastic scattering cross section

S. Alsalmi (spokesperson)

*King Saud University, Riyadh 11451, Saudi Arabia*

E. Fuchey (spokesperson) and A.J.R. Puckett

*University of Connecticut, Storrs, Connecticut 06269, USA*

B. Wojtsekowski (spokesperson), S. Barcus\*, A. Camsonne\*, J-P. Chen\*,  
D. Gaskell\*, O. Hansen, D. W. Higinbotham, M. Jones, C. Keppel\*, D. Mack\*,  
D. Meekins, R. Michaels, B. Sawatzky, G. Smith, A. Tadepalli, and S. Wood\*  
*Thomas Jefferson National Accelerator Facility, Newport News, Virginia 23606, USA*

K. Aniol

*California State University, Los Angeles, CA 90032, USA*

J. Arrington and P. Reimer\*

*Argonne National Laboratory, 9700 S Cass Ave, Lemont, Illinois 60439, USA*

T. Averett

*The College of William and Mary, Williamsburg, Virginia 23185, USA*

V. Bellini\*

*Istituto Nazionale di Fisica Nucleare, I-95123 Catania, Italy*

J. Bernauer\*

*Stony Brook University, Stony Brook, NY 11794, US*

W. Boeglin and P. Markowitz

*Florida International University, Miami, FL 33199, USA*

G. Cates\*, K. Gnanvo\*, C. Gu\*, J. Liu\*, N. Liyanage\*, V. Nelyubin\*, and C. Palatchi\*

*University of Virginia, Charlottesville, Virginia 22904, USA*

E. Cisbani, F. Meddi\*, and G. Urciuoli\*

*Istituto Nazionale di Fisica Nucleare - Sezione di Roma,*

*P.le Aldo Moro, 2 - 00185 Roma, Italy*

J.C. Cornejo\* and B. Quinn\*

*Carnegie Mellon University, Pittsburgh, Pennsylvania 15213, USA*

B. Crowe\* and B. Vlahovic\*

*North Carolina Central University, Durham, North Carolina 27707, USA*

C. Gayoso

*Mississippi State University, Mississippi State, MS 39762, USA*

D. Hamilton and R. Montgomery

*SUPA School of Physics and Astronomy,*

*University of Glasgow, Glasgow G12 8QQ, UK*

F. Hauenstein

*Old Dominion University, Norfolk, Virginia 23529, USA*

A. T. Katramatou and G.G. Petratos

*Kent State University, Kent, OH 44242, USA*

D. Nguyen

*Massachusetts Institute of Technology, Cambridge, MA 02139, USA*

C. Petta\* and C. Suttera\*

*Istituto Nazionale di Fisica Nucleare, Dipt. di Fisica dell Univ. di Catania, I-95123 Catania, Italy*

A. Sarty

*Saint Mary's University, Halifax, Nova Scotia B3H 3C3, Canada*

A. Schmidt

*The George Washington University, Washington, DC 20052, USA*

K. Slifer\*

*University of New Hampshire, Durham, NH 03824, USA*

A. Shahinyan

*AANL, 2 Alikhanian Brothers Street, 0036, Yerevan, Armenia*

S. Širca\*

*Faculty of Mathematics and Physics, University of Ljubljana, 1000 Ljubljana, Slovenia*

W. Tireman

*Northern Michigan University, Marquette, Michigan 49855, USA*

E. Voutier\*

*Institut de Physique Nucléaire, 15 Rue Georges Clemenceau, 91400 Orsay, France*

(Dated: June 14, 2020)

## Abstract

We propose to make a high precision measurement of the two-photon exchange contribution (TPE) in elastic electron-neutron scattering at a four-momentum transfer  $Q^2 = 4.5$   $(\text{GeV}/c)^2$ . While significant efforts to study the two-photon-exchange have focused around elastic electron-proton scattering, the impact of TPE on neutron form factors was never examined experimentally. The proposed experiment will provide the very first assessment of the two-photon exchange in electron-neutron scattering, which will be important for understanding the nucleon form factor physics.

The proposed experiment will be performed in Hall A using the BigBite (BB) spectrometer to detect the scattered electrons and the Super-BigBite (SBS) to detect the protons and neutrons. The experiment should run concurrently with the E12-09-019  $G_M^n$  and E12-17-004  $G_E^n$ -Recoil experiments, which are expected to run in 2021. The experimental setup of the proposed experiment will be identical to that of E12-09-019 experiment.

The “ratio” method will be used to extract the electric form factor of the neutron  $G_E^n$  by scattering unpolarized electrons from deuterium quasi-elastically at two beam energies 4.4 and 6.6 GeV and electron scattering angles 41.9 and 23.3 degrees respectively. In the proposed approach, systematic errors are greatly reduced compared to those in the traditional single electron arm configuration. Several experiments at Mainz and JLab have used the ratio method to measure the neutron magnetic form factor in the past years. The method can be extended to extract the neutron electric form factor even with less stringent requirements on the knowledge of the absolute neutron detection efficiency and experimental kinematics.

## I. INTRODUCTION

In 1950's, a series of experiments performed by R. Hofstadter [1] revealed that the nucleons have a substructure (would be called later the quarks and gluons). The experiment confirmed M. Rosenbluth's theory [2] based on one-photon exchange approximation. In the Born approximation, where the interaction between the electron and the nucleon occurs *via* an exchange of a one virtual photon (OPE), the unpolarized  $e - N$  elastic cross section can be expressed in terms of a nucleon magnetic,  $G_M$ , and electric,  $G_E$ , form factors. These form factors describe the deviation from a point-like scattering cross section:

$$\left( \frac{d\sigma}{d\Omega} \right)_{eN \rightarrow eN} = \frac{\sigma_{Mott}}{\epsilon(1 + \tau)} [\tau \cdot G_M^2(Q^2) + \epsilon \cdot G_E^2(Q^2)], \quad (1)$$

where  $E$  and  $E'$  are the incident and scattered electron energies, respectively,  $\theta$  is the electron scattering angle,  $\tau \equiv -q^2/4M^2$ , with  $-q^2 \equiv Q^2 = 4EE' \sin(\theta/2)$  being the negative four momentum transfer square,  $M$  is the nucleon mass, and  $\epsilon = [1 + 2(1 + \tau) \tan^2(\theta/2)]^{-1}$  is the longitudinal polarization of the virtual photon. The reduced cross section is defined by:

$$\sigma_r \equiv \left( \frac{d\sigma}{d\Omega} \right) \cdot \frac{\epsilon(1 + \tau)}{\sigma_{Mott}} = \tau \cdot G_M^2(Q^2) + \epsilon \cdot G_E^2(Q^2) = \sigma_T + \epsilon \cdot \sigma_L, \quad (2)$$

where  $\sigma_L$  and  $\sigma_T$  are the cross sections for longitudinally and transversely polarized virtual photons, respectively.

The linear  $\epsilon$  dependence of the cross section is due to  $\sigma_L$  term, see Eq. 1. The ratio  $\sigma_L/\sigma_T$  is a Rosenbluth slope related to  $G_E/G_M$  (in OPE), see Fig. 1. The data show that at  $Q^2$  of 4-5  $(\text{GeV}/c)^2$  the Rosenbluth slope is three-four times larger than it suppose to be (in OPE) for the observed values of the  $G_E^p/G_M^p$  ratio.

The nucleon electromagnetic form factors can reveal a lot of information about the nucleon internal structure, as well as the quark distribution. The form factors depend only on one



FIG. 1. The square root of Rosenbluth slope, corrected for kinematical factor  $\sqrt{\tau}$  and  $\mu_p$ , observed in elastic electron-proton scattering, adopted from Ref. [3].

variable the negative square of the four-momentum transfer carried by the photon,  $Q^2$ . In the limit of large  $Q^2$ , pQCD provides well-motivated predictions for the  $Q^2$ -dependance of the form factors and their ratio. However, it was never predicted at what  $Q^2$  range the pQCD prediction (scaling) will be valid. Studies of GPDs show that pQCD validity will require a very large  $Q^2$  of 100  $(\text{GeV}/c)^2$ . It was discovered at JLab, using the double polarization methods, that the proton electric and magnetic form factors behave differently starting at  $Q^2 \approx 1 (\text{GeV}/c)^2$ .

Experimentally, the nucleon form factors can be measured using one of two techniques: polarization transfer technique and Rosenbluth technique. The polarization method examines the polarization transfer from longitudinally polarized electron to the recoiling nucleon and determine the resulting azimuthal asymmetry distribution using a polarimeter. Alternatively, one can use the polarized electron beam and a polarized target. While in the Rosenbluth method, the electric and magnetic form factors can be separated by making two or more measurements with different  $\epsilon$  values (*i.e.* different beam energies and angles), but with same  $Q^2$  value. Rosenbluth technique requires an accurate measurement of the

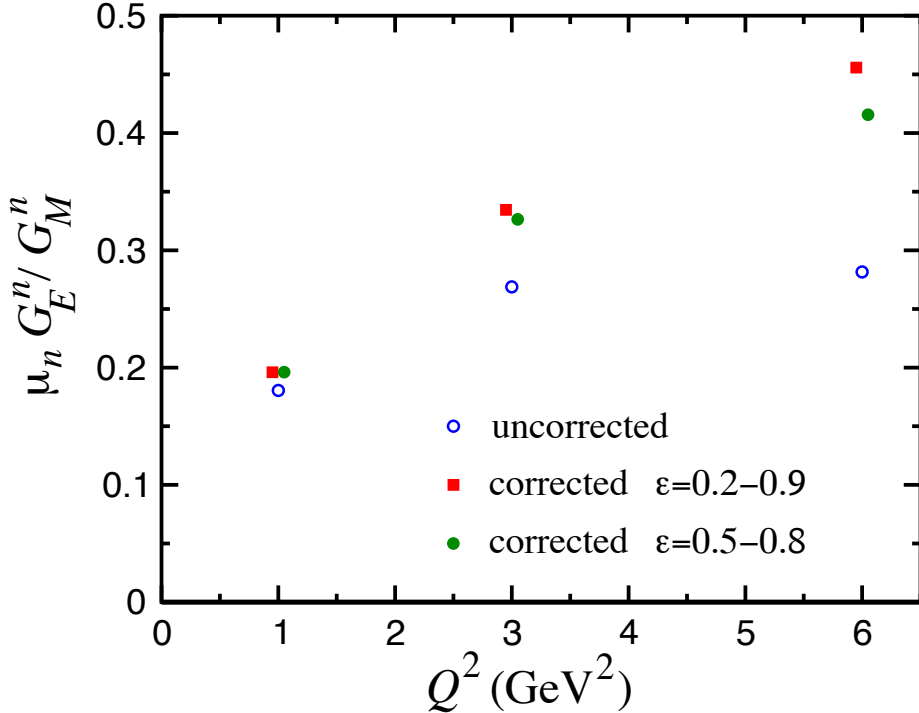


FIG. 2. Projected impact of TPE on  $G_E^n/G_M^n$  using LT separation, according to Ref. [4].

cross section and suffers from large systematic uncertainties arising from several factors. For instance, an accurate knowledge of the neutron detector efficiency is required.

When comparing the values of  $G_E^p/G_M^p$  obtained from both techniques, a significant discrepancy was observed (see Fig. 1). Such discrepancy implies a potential problem in our understanding of the nucleon substructure. Many efforts were made in order to provide legitimate explanation, and it is believed that the inconsistency is due to contribution of two-photon exchange in  $e - N$  elastic scattering process, see Refs. [5, 6]. Predictions made for the neutron case are shown in Fig. 2, adopted from [4]. The contribution of TPE could reach about 30% of Rosenbluth slope value at 5 (GeV/c) $^2$ .

In the following we propose to make precision L/T separation of the elastic electron-neutron cross section and first experimental assessment of the two-photon exchange contribution on the neutron magnetic form factor measurements (see also Ref. [7]). The result of

50 the nTPE experiment will likely add a new component to our understanding of the elastic  
51 electron-nucleon process.

52

## II. PHYSICS MOTIVATION

53      The nucleon plays the same central role in hadronic physics that the hydrogen atom does  
 54      in atomic physics and the deuteron in the physics of nuclei. The structure of the nucleon  
 55      and its specific properties, such as charge, magnetic moment, size, mass; the elastic electron  
 56      scattering form factors, resonances; and structure functions in DIS, are of fundamental sci-  
 57      entific interest. The isospin is a fundamental property of the nucleon, so both the proton and  
 58      neutron investigations are important to do. By using data on the proton and neutron form  
 59      factors the flavour structure could be explored [8]. It is already provided the most direct  
 60      evidence for a diquark correlation in the nucleon [9–11].

61      Hadron structure, as seen in elastic electron scattering, in one-photon approximation,  
 62      defined by two functions of four momentum transfer square. They are: the helicity conserving  
 63      Dirac form factor,  $F_1$ , which describes the distribution of the electric charge, and the helicity  
 64      non-conserving Pauli form factor,  $F_2$ , describes the distribution of the magnetic moment.  
 65      These two form factors are the ingredients of the hadronic current. These form factors  
 66      contain information on the transverse charge distribution for an unpolarized and transversely  
 67      polarized nucleon, respectively, in the infinite momentum frame [12, 13].

68      The Sachs form factors,  $G_E$  and  $G_M$ , the ratio of which will be extracted directly from  
 69      the data, are related to  $F_1$  and  $F_2$  by

$$F_1 = \frac{G_E + \tau G_M}{1 + \tau} \text{ and } F_2 = \frac{G_M - G_E}{\kappa(1 + \tau)}, \quad (3)$$

70      where  $\kappa$  is the nucleon anomalous magnetic moment.

71      Already twenty four years ago, important developments in QCD phenomenology has  
 72      been the exploration of the generalized parton distribution (GPD) formalism [14–16], which  
 73      provides relations between inclusive and exclusive observables. The nucleon elastic form  
 74      factors  $F_1$  and  $F_2$  are given by the first moments of the GPDs

$$F_1(t) = \sum_q \int_0^1 H^q(x, \xi, t, \mu) dx \text{ and } F_2(t) = \sum_q \int_0^1 E^q(x, \xi, t, \mu) dx, \quad (4)$$

75      where  $H^q$  and  $E^q$  are two of the generalized parton distributions,  $x$  is the standard Bjorken  
 76       $x$ ,  $\xi$  is the “skewness” of the reaction,  $t$  is the four-momentum transferred by the electron,

<sup>77</sup>  $\mu$  is a scale parameter necessary from the evolution over  $Q^2$ , analogous to DIS parton dis-  
<sup>78</sup> tributions, and the sum is over all quarks and anti-quarks. These may be accessed through  
<sup>79</sup> processes such as deeply virtual Compton scattering, where the interaction is factorized into  
<sup>80</sup> a hard part with the virtual photon/photon interactions with an individual quark and a soft  
<sup>81</sup> part of the residual system where the GPD information is contained.

<sup>82</sup> Fundamental nucleon feature, the spin, is related to GPDs, as shown by X. Ji [15]. The  
<sup>83</sup> moments of GPDs can yield information, according to the Ji's Angular Momentum Sum  
<sup>84</sup> Rule, on the contribution to the nucleon spin from quarks and gluons, including both the  
<sup>85</sup> quark spin and orbital angular momentum.

<sup>86</sup> At present, experimental measurements of GPDs are still scarce. Until high  $Q^2$  DVCS  
<sup>87</sup> data becomes available, work has been done to attempt to parameterize these GPDs, which  
<sup>88</sup> rely heavily on data from electromagnetic form factors and parton distributions from DIS as  
<sup>89</sup> constraints [17]. Data at high  $Q^2$  for  $G_E^n$  would contribute significantly in the development  
<sup>90</sup> of these models.

<sup>91</sup> As we presented above the form factors are important components for GPDs development.  
<sup>92</sup> However, the cross section of elastic  $e-p$  scattering contains a significant contribution to  $\sigma_L$ ,  
<sup>93</sup> which at high  $Q^2$  is much larger than theory calculations expected [18]. Such an alarming  
<sup>94</sup> observation underlines that understanding of TPE effect is essential for hadron physics.

95

### III. TECHNIQUE

96 This proposal is based on instrumentation, simulation, and analysis development made  
 97 by the GMn/SBS collaboration for the GMn, E12-09-019, experiment [19]. The GMn experi-  
 98 ment is one of several form factor experiments approved by JLab PAC. The SBS spectrometer  
 99 was funded by DOE with large contributions provided by the collaborating institutions from  
 100 USA, Italy, UK, and Canada. The apparatus and DAQ installation will start in 2020 and  
 101 the data taking run is expected to be in summer-fall 2021.

102 The neutron form factors are challenging to be determine experimentally especially be-  
 103 cause there is no free neutron target. However, since the deuterium is a loosely coupled  
 104 system, it can be viewed as the sum of a proton target and a neutron target. In fact, quasi-  
 105 elastic scattering from deuterium has been used to extract the neutron magnetic form factor,  
 106  $G_M^n$ , at modestly high  $Q^2$  for decades [20, 21] in the single arm ( $e, e'$ ) experiments. How-  
 107 ever, the proton cross section needs to be subtracted by applying a single-arm quasi-elastic  
 108 electron-proton scattering. This “proton-subtraction” technique suffers from a number sys-  
 109 tematic uncertainties e.g. contributions from inelastic and secondary scattering processes.

110 Many year ago, L. Durand [22] proposed the so-called “ratio-method” based on the mea-  
 111 surement of both  $D(e, e'n)$  and  $D(e, e'p)$  reactions. In this method, many of the systematic  
 112 errors are cancel out. Several experiments [23–25] have applied the ratio-method to deter-  
 113 mine the neutron magnetic form factor.

114 The GMn/SBS experiment [19] will take data for elastic  $e - n$  scattering for several  
 115 kinematics with  $Q^2$  from 3.5 up to 13.5  $(\text{GeV}/c)^2$ . We propose to use this method to  
 116 measure Rosenbluth slope and extract (in OPE approximation) the neutron electric form  
 117 factor,  $G_E^n$ , at one value of momentum transfer. In fact, one of required data points will  
 118 be taken by the GMn experiment, so an additional measurement is needed only for one  
 119 kinematics.

120 Data will be collected for quasi-elastic electron scattering from deuteron in process  
 121  $D(e, e'n)p$ . A complementary  $D(e, e'p)n$  data will be taken to calibrate the experiment ap-  
 122 paratus. The current knowledge of the  $e - p$  elastic scattering cross section (obtained in the  
 123 single arm  $H(e, e')p$  and  $H(e, p)e'$  experiments) will be also used for precision determination

<sup>124</sup> the experiment kinematics.

<sup>125</sup> Applying Rosenbluth technique to measure  $G_E^n$  requires accurate measurement of the cross  
<sup>126</sup> section and suffers from large uncertainties. To overcome this issue, we propose to extract  
<sup>127</sup> the value of  $G_E^n$  from the ratio of quasi-elastic yields,  $R_{n/p}$ , in scattering from a deuteron  
<sup>128</sup> target as follows:

$$R_{n/p} \equiv R_{observed} = \frac{N_{e,e'n}}{N_{e,e'p}} \quad (5)$$

<sup>129</sup>  $R_{observed}$  needs to be corrected to extract the ratio of e-n/e-p scattering from nucleons:

$$R_{corrected} = f_{corr} \times R_{observed} , \quad (6)$$

<sup>130</sup> where the correction factor  $f_{correction}$  takes into account the variation in the hadron efficiencies  
<sup>131</sup> due to changes of  $e - N$  Jacobian, the radiative corrections, and absorption in path from the  
<sup>132</sup> target to the detector, and small re-scattering correction.

<sup>133</sup> In one-photon approximation,  $R_{corrected}$  can be presented as:

$$R_{corrected} = \frac{\sigma_{Mott}^n \cdot (1 + \tau_p)}{\sigma_{Mott}^p \cdot (1 + \tau_n)} \times \frac{\epsilon \sigma_L^n + \sigma_T^n}{\epsilon \sigma_L^p + \sigma_T^p} \quad (7)$$

It is important that the ratio  $R_{Mott} = \frac{\sigma_{Mott}^n \cdot (1 + \tau_p)}{\sigma_{Mott}^p \cdot (1 + \tau_n)}$  could be determine with very high relative accuracy even with modest precision for the beam energy, electron scattering angle, and detector solid angle. Now, let us write the  $R_{corrected}$  at two values of  $\epsilon$  using  $R_c^{n(p)} = \sigma_L^{n(p)} / \sigma_T^{n(p)}$  as:

$$R_{corrected,\epsilon_1} = R_{Mott,\epsilon_1} \times \frac{\epsilon_1 \sigma_L^n + \sigma_T^n}{\epsilon_1 \sigma_L^p + \sigma_T^p} \quad R_{corrected,\epsilon_2} = R_{Mott,\epsilon_2} \times \frac{\epsilon_2 \sigma_L^n + \sigma_T^n}{\epsilon_2 \sigma_L^p + \sigma_T^p}$$

In these two equations there are two unknown variables:  $\sigma_L^n$  and  $\sigma_T^n$ . The dominant contribution to the uncertainty of the slope of the cross section vs.  $\epsilon$ ,  $S_c^n = \sigma_L^n / \sigma_T^n$ , will come from the uncertainty of  $S_c^p$ . At  $Q^2=4.5$  (GeV/c)<sup>2</sup>, according to the global analysis of  $e - p$  cross section [3], the value of  $S_c^p$  is close to  $1/(\tau \mu_p^2) = 0.107$  with uncertainty of 0.01. The resulting equation for  $S_c^n$  is:

$$A = B \times \frac{1 + \epsilon_1 S_c^n}{1 + \epsilon_2 S_c^n} \approx B \times (1 + \Delta \epsilon \cdot S_c^n),$$

where the variable  $A = R_{corrected,\epsilon_1}/R_{corrected,\epsilon_2}$  will be measured with relative precision of 0.1%. Assuming, for this estimate, equal values of  $Q^2$  for two kinematics, the  $\tau$  and  $\sigma_T$  for two kinematics are canceled out, and the variable  $B = R_{M,\epsilon_1}/R_{M,\epsilon_2} \times (1 + \epsilon_2 S_c^p)/(1 + \epsilon_1 S_c^p)$ . For actual small range of  $\epsilon$  and small value of the slope, the  $B \approx (1 - \Delta\epsilon \cdot S_c^p)$ . The value of  $B$  will be determined from global proton  $e - p$  data to a precision of  $0.25 \times 0.01$ .

At  $Q^2=4.5$  (GeV/c)<sup>2</sup> the ratio  $\mu_n G_E^n/G_M^n$  is of  $0.55 \pm 0.05$ , see the review [26]. In a simplest model, the slope  $S_c^n$  is a sum of the slope due to  $G_E^n/G_M^n$  and the TPE contribution. If we use for TPE the prediction [4], shown in Fig. 2, the TPE leads to increase of  $S_c^n$  by a factor of 2, so the result of this experiment for TPE will be  $0.069 \pm 0.012 \pm 0.01$ , where the first uncertainty is due to accuracy of  $G_E^n/G_M^n$  and the second one due to projected precision of this experiment. It would be a 4-4.5 sigma observation of the neutron TPE.

145

#### IV. EXPERIMENTAL SETUP

146 As illustrated in Fig. 3, this experiment will study electron scattering from a 15 cm  
 147 long liquid Deuterium target held in a vacuum. The scattered electron will be detected  
 148 in the BigBite spectrometer with an upgraded electron detector stack. The neutron arm is  
 149 arranged with a dipole magnet 48D48 (SBS) and a segmented hadron calorimeter HCAL. The  
 150 whole detector package was designed and is now under assembling for the GMn, E12-09-019,  
 151 experiment.

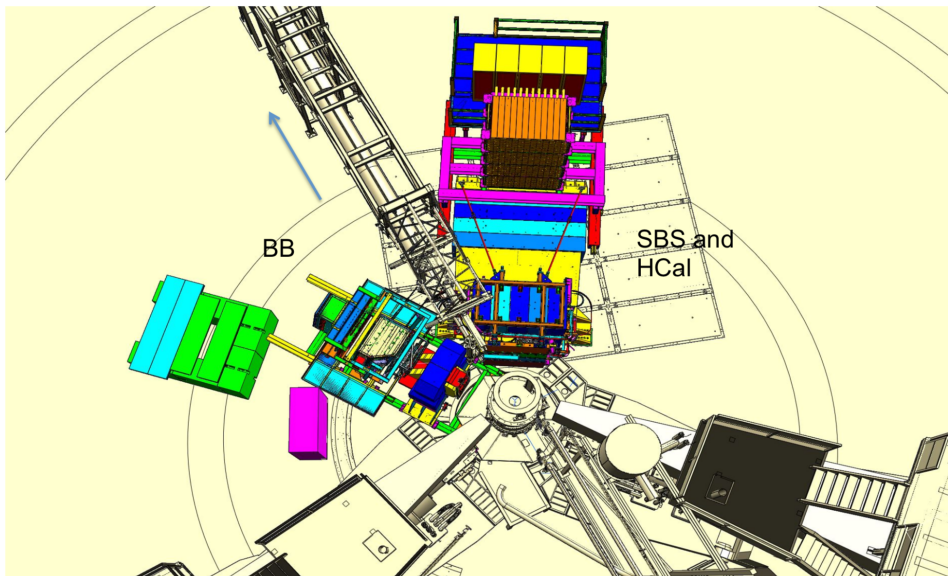


FIG. 3. Layout of the experimental setup in nTPE.

152

##### 1. Parameters of the SBS

153 The 48D48 magnet from Brookhaven was acquired as part of the Super Bigbite project  
 154 and will be available for this experiment. It consists of a large dipole magnet which provides  
 155 a field integral of about  $1.7 \text{ T} \cdot \text{m}$ , allowing for quasielastic protons to be sufficiently deflected  
 156 to allow clear differentiation from neutrons. The active field volume has an opening of  $46 \times$   
 157  $25 \text{ vertical} \times \text{horizontal}$ ), matching the aspect ratio of the neutron arm, and a depth of 48  
 158 cm.

159     The placement of this magnet will be 1.6 m away from the target, which would normally  
160    interfere with the beamline. To accommodate this, modifications were made to the iron yoke  
161    such that the beamline will pass through the magnet yoke area.

162     The field configuration will be such that positively charged particles will be deflected  
163    upwards away from the hall floor. For a field integral of 1.7 Tesla-m, protons of momentum  
164    2.5 GeV/c will be deflected 250 mrad, which translates to a displacement of xxm. Including  
165    expected detector resolution, the  $p_{miss,\perp}$  distribution will be similar to what was seen in  
166    E02-013, so cuts of < 100 MeV/c will be appropriate. Monte Carlo simulations show a  
167    contamination of charged quasielastics to be negligible.

168     The presence of the magnet also works to sweep low energy charged particles from the  
169    target away from the neutron arm. Particles of momentum less than 1.3 GeV/c will be  
170    entirely swept outside of the neutron arm acceptance. This greatly reduces the amount of  
171    charged low energy background.

172

### A. The BigBite Spectrometer

173 Scattered electrons will be detected in the BigBite spectrometer. The spectrometer con-  
 174 sists of a single dipole magnet (with magnetic field approximately 1.2 T) and a detection  
 175 system, see Fig. 4.

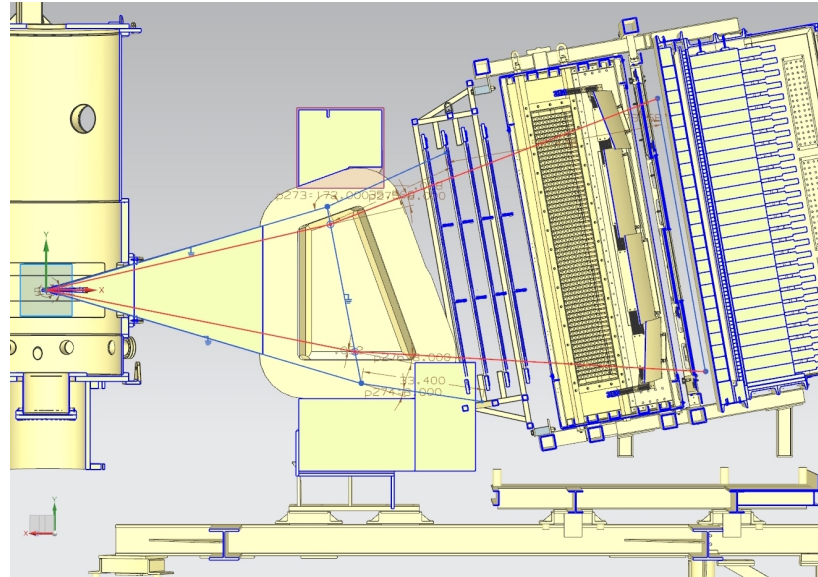


FIG. 4. The BigBite spectrometer with the upgraded detector stack.

176

#### 1. GEM Chambers

177 To perform the tracking of charged particles under the high rates anticipated for this  
 178 experiment, the drift chambers were replaced with gas electron multiplier (GEM) detectors.  
 179 These detectors have proven to be capable of operating under luminosities of  $25 \text{ kHz/mm}^2$   
 180 for the COMPASS experiment at CERN and the spatial resolution of each of these chambers  
 181 is anticipated to be about  $70 \mu\text{m}$ . There will be two sets of GEMs placed on each side of the  
 182 GRINCH Cherenkov detector.

183 The set of GEMs in front of the GRINCH is composed of four layers of GEMs. Two of  
 184 these layers have been built by will the SBS collaborators from INFN. They are composed

185 three modules each, measuring  $40 \times 50 \text{ cm}^2$ , such that each layer covers  $40 \times 150 \text{ cm}^2$  (the  
 186 long dimension being vertical, along the dispersive direction). The readout of these modules  
 187 are oriented in the  $x/y$  direction *i.e.* parallel and perpendicular to the dispersive direction  
 188 (horizontal and vertical). The two other layers are being built by the SBS collaborators from  
 189 UVA. They are composed of a single module measuring  $40 \times 150 \text{ cm}^2$ , the long dimension  
 190 again being vertical and along the dispersive direction. The readout of these modules are  
 191 oriented in the  $u/v$  direction *i.e.*  $\pm 30$  degrees with respect to the horizontal direction.

192 The set of GEMs behind the GRINCH has been built by the SBS collaborators from  
 193 UVA. It is composed of a single layer composed of four modules measuring  $50 \times 60 \text{ cm}^2$ ,  
 194 such that the layer covers  $60 \times 200 \text{ cm}^2$  (the long dimension again being along the dispersive  
 195 direction). The readout of these modules are all oriented in the  $x/y$  direction.

196 The level background in the GEMs have been evaluated, thanks to G4SBS ([27] abd  
 197 Sec. V) for the  $G_M^n$  experimental readiness review. For the  $G_M^n$  highest  $Q^2$  point (which is the  
 198 most constraining, since it combines mandatory maximum luminosity and smaller BigBite  
 199 angles, the background level in the front GEMs are of the order of  $120 \text{ kHz/cm}^2$  for the front  
 200 GEM layers, and below  $50 \text{ kHz/cm}^2$  for the back GEM. To perform the GEM tracking within  
 201 such a background environment, we use the cluster reconstructed in the BigBite shower as  
 202 a track seed to clean the large combinatorics that would otherwise be created by the large  
 203 number of hits. After this, the main challenge is the separation by the clustering algorithm  
 204 of the signal and background hits to minimize track smearing. At this level of background, a  
 205 TreeSearch tracking algorithm combined with a fairly simple cluster separation algorithm has  
 206 already proven to achieve 70% efficiency at nominal luminosity. A better cluster separation  
 207 algorithm is currently being developed and should allow to significantly improve this figure.

208

## 2. Shower/Preshower

209 The electromagnetic calorimeter configuration consists of two planes of lead glass blocks  
 210 which we call the preshower and shower. The preshower, located about 80 cm behind  
 211 the first GEM chamber, consists of a  $2 \times 26$  plane of  $37 \text{ cm} \times 9 \text{ cm}$  blocks. The shower, about  
 212 1 m behind the first GEM chamber, consists of an  $7 \times 27$  array of  $8.5 \text{ cm} \times 8.5 \text{ cm}$  blocks.

213 Sums over these blocks form the physics event trigger for the experiment.

214 The preshower signal can be used to provide an additional method of pion rejection.  
215 By selecting low preshower signals, a pion rejection factor of 1:50 can be achieved through  
216 optimization. Despite higher particle rates, pion rejection performance is anticipated to  
217 be similar to that achieved for Transversity, E06-010. By measuring the pedestal widths  
218 and resolution for E06-010 and scaling to this proposal's conditions, overall relative energy  
219 resolution for the detector is expected to become worse by a factor of 1.6, to about  $\sigma_{\delta E/E} =$   
220 25%.

### 221 3. Timing hodoscope

222 The BigBite timing hodoscope has been built the the SBS collaborators from Glasgow,  
223 to replace the BigBite scintillator plane. It will be composed of 90 bars stacked in a plane,  
224 each with dimensions 1 in.  $\times$  1 in.  $\times$  60 cm. The paddle stack will be oriented such as  
225 the long dimension of the bars is horizontal *i.e.* perpendicular to the dispersive direction.  
226 Each of these elements are readout by a PMT on each side, mostly to provide measurement  
227 redundancy.

228 This plane will primarily be used to provide a signal for nucleon time of flight reconstruc-  
229 tion. A time resolution of 200 ps is anticipated. This fine segmentation is meant to lower the  
230 rates in the detector. Background studies made for the  $G_M^n$  experimental readiness review  
231 demonstrated that the rates experienced by each element was  $\leq$  500 kHz at a luminosity of  
232  $2.8 \times 10^{38}$  cm $^{-2}$  s $^{-2}$ . The PMTs pulses are processed by NINO front-end cards which, when  
233 the PMT pulse crosses the NINO threshold, will produce a digital signal to be readout by  
234 CAEN 1190 TDCs which record a leading time and a trailing time.

### 235 4. GRINCH cherenkov detector

236 The main purpose of the Ring Imaging Cherenkov is to provide additional particle iden-  
237 tification for offline pion rejection. The GRINCH consists of a tank with a maximum depth  
238 of 88.9 cm, with 4 cylindrical mirrors focussing the cherenkov light directly onto a 510 PMT

<sup>239</sup> array (60 lines of PMTs, with lines of 9 PMTs alternating with lines of 8 PMTs) placed away  
<sup>240</sup> from the beam. The radiation gas will be  $C_4F_8$ , which is by far the best compromise between  
<sup>241</sup> light yield for electrons and operating cost. With  $n - 1 = 1.35 \times 10^{-3}$ , the  $\pi$  threshold is only  
<sup>242</sup> about 2.7 GeV, so the additional pion rejection will be most effective below this threshold.

<sup>243</sup> As for the timing hodoscope The PMTs pulses are processed by NINO front-end cards  
<sup>244</sup> which, when the PMT pulse crosses the NINO threshold, will produce a digital signal to  
<sup>245</sup> be readout by VETROC TDCs, which for each PMT hit will record a leading time and a  
<sup>246</sup> trailing time. The analog signal will not be recorded however, which means that for each  
<sup>247</sup> PMT hit, the information of the number of not directly available (although it can in theory  
<sup>248</sup> be deduced from the time over threshold).

<sup>249</sup> All of this implies that the electron selection relies on the number of GRINCH PMT  
<sup>250</sup> firing, instead of relying on the signal amplitude.

251

## B. Hadron Calorimeter (HCal)

252 The Hadron Calorimeter (HCal) has been designed specifically to measure the recoil  
 253 nucleon for the SBS experiments. Specifically for this experiment (and for  $G_M^n$ ), HCal  
 254 combined with the SBS (48D48) magnet provides identification of the recoil nucleon, as  
 255 well as additional kinematic constraint and possibly timing information on the measured  
 256 interaction. Nucleon identification is illustrated on Fig. 5. This figure shows the compared  
 257 proton and neutron position distribution in HCal at the same electron kinematics. The  
 258 proton distribution is being shifted upwards by about 1 m compared to the neutron.

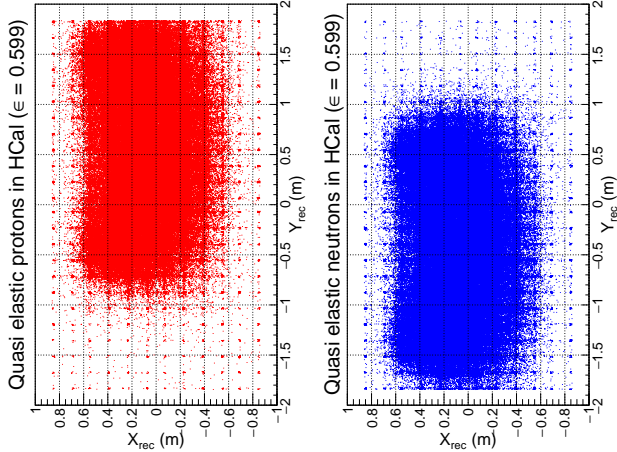


FIG. 5. Reconstructed HCal cluster from quasi-elastic events generated by G4SBS. The left distribution in red is for the proton, the right distribution in blue is for the neutron.

259

260

261 The HCal (which CAD model is shown on Fig. 6) is composed of 288 modules arranged in  
 262 an array of  $12 \times 24$ . In front of the full assembly is located a  $3/4$  in steel plate which purpose  
 264 is double:

- 265 • initiate the hadronic shower to optimize the calorimeter response;
  - 266 • shield the modules from a fraction of the low energy secondaries;
- 267 Each of these modules measures  $6 \times 6 \text{ in}^2$  section, for 3 ft length. They are composed of  
 268 alternating tiles of scintillators and iron around a central light guide which collects the light

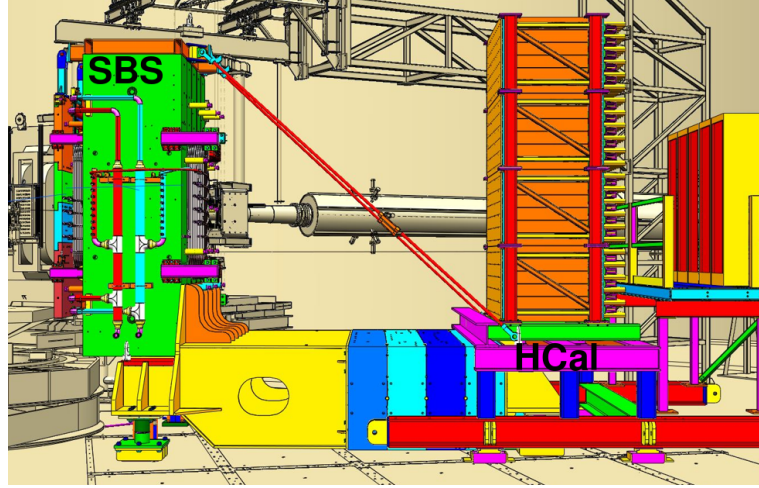


FIG. 6. CAD representation of HCal (right) with the SBS magnet (left)

<sup>269</sup> generated in the scintillators by the hadronic shower, and guides it to the PMT at the end of  
<sup>270</sup> the block. Cosmics tests have determined that the average light yield for the HCal modules  
<sup>271</sup> is around 5 photoelectrons per MeV deposited in the scintillator tiles.

<sup>272</sup> The PMTs are readout with FAD250 which sample the PMT signal every 40 ns and allow  
<sup>273</sup> to reconstruct the PMT pulse shape, hence its timing. They are also readout by TDCs which  
<sup>274</sup> provide additional timing information. Thanks to this, the timing resolution can be better  
<sup>275</sup> than 1 ns, which cosmics tests (in progress) seem to confirm.

<sup>276</sup> The energy resolution is intrinsically broad (see Fig. 9 in Section V), due mostly to the  
<sup>277</sup> small fraction of energy from the hadronic shower actually measured by the scintillator tiles  
<sup>278</sup> ( $\leq 0.1$  - refer yet again to Fig. 9).

279       **V. SIMULATIONS, ESTIMATIONS OF COUNTING RATES AND**  
 280       **ACCIDENTALS**

281       The estimations of counting rates accidentals have been performed using G4SBS, the  
 282       GEANT4-based simulation package developed for the SBS experiment [27]. This package  
 283       includes a wide range of event generators, which allows to evaluate the rates for both events  
 284       of interest (signal) and background. The representation of the experiment apparatus in  
 285       G4SBS is shown in the high  $\epsilon$  configuration on Fig. 7.

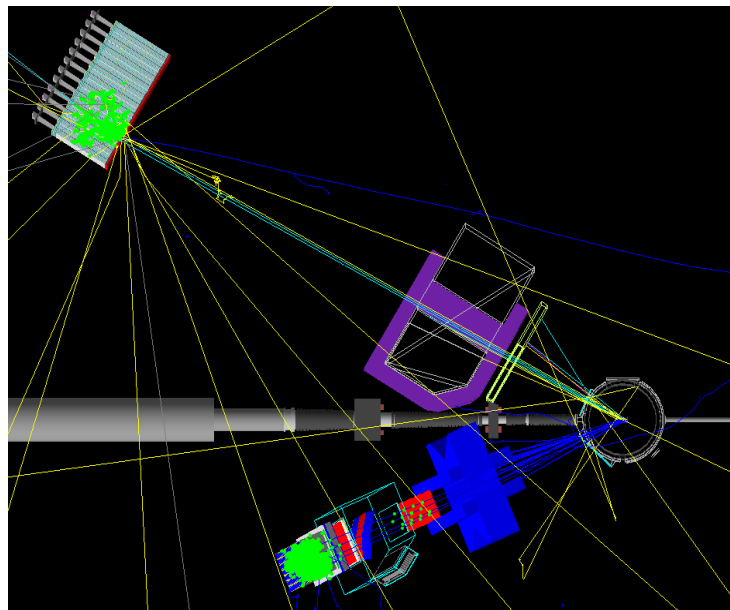


FIG. 7. Top view of the experimental apparatus model in G4SBS, shown in the high  $\epsilon$  configuration. The beam direction is indicated, as well as the main elements (HCAL, SBS magnet, BigBite spectrometer)

286  
 287       **A. Background and trigger rates**

289       The main processes expected to contribute the trigger rates for the BigBite spectrometer  
 290       are:

291 • the inelastic electron nucleon scattering process;

292 • photons from inclusive  $\pi^0$  production;

293 • and to a lesser extent, charged pions.

294 One the other hand, we expect all sorts of hadronic backgrounds to contribute to the rates in  
 295 HCal, the dominant ones being pions. Both the inelastic scattering and the inclusive neutral  
 296 and charged pion production are implemented in G4SBS, the latter relying on the Wiser  
 297 parametrization [28]. We may also considered the minimum-bias “beam-on-target” gener-  
 298 ator for the HCal background, especially at lower angle (all electromagnetic and hadronic  
 299 processes being built-in in G4SBS).

300 The thresholds to apply to each arm are determined as a function of the elastic peak. For  
 301 the electron arm, the threshold has been set at  $\mu_E - 2.5\sigma_E$ ,  $\mu_E$  and  $\sigma_E$  being respectively  
 302 the position and width of the fitted elastic peak. Fig. 8 presents the distributions of rate of  
 303 energy deposit for the different processes involved in the BigBite trigger rates.

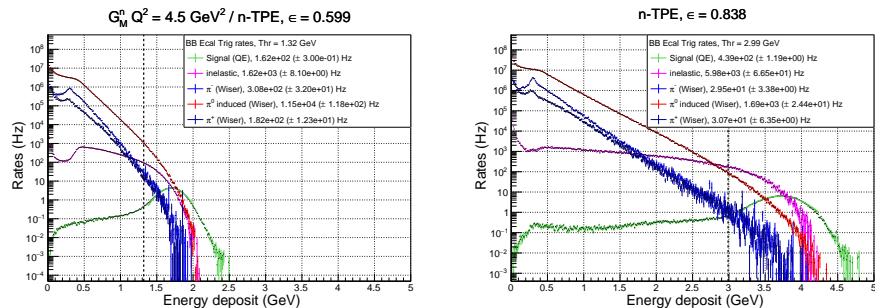


FIG. 8. Rates of the different process contributing to the BigBite electron arm trigger, for the low  $\epsilon$  (left) and the high  $\epsilon$  (right). Quasi-elastic is in green, inelastic in magenta,  $\pi^0$  in red,  $\pi^-$  in blue, and  $\pi^+$  in dark blue. Note the resolution for the elastic peak in the BigBite shower is  $\sim 0.3$  GeV.

304

305

306 Since HCal is a sampling calorimeter (meaning that only a fraction of the shower energy  
 307 is measured), it's resolution is significantly wider ( $\sim 0.7$  GeV). Due to this, the threshold  
 308 is at 90% efficiency (which corresponds to  $\sim 0.1$  GeV for both kinematics. Fig. 9 presents

309 the distributions of rate of energy deposit for the different processes involved in the BigBite  
 310 trigger rates.

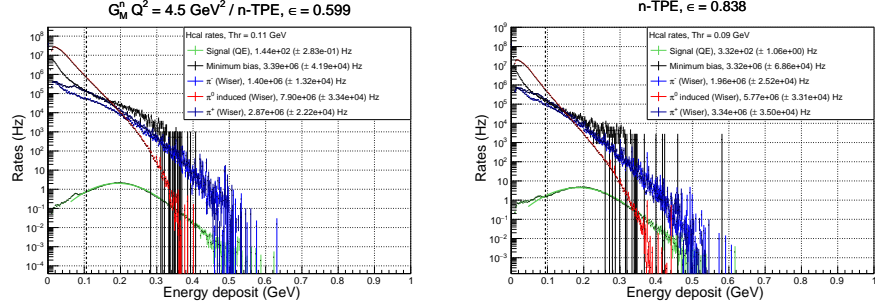


FIG. 9. Rates of the different process contributing to the HCal trigger, for the low  $\epsilon$  (left) and the high  $\epsilon$  (right). Quasi-elastic is in green, minimum bias in black,  $\pi^0$  in red,  $\pi^-$  in blue, and  $\pi^+$  in dark blue. Note the peak itself is around 0.2 GeV for 3.2 GeV nucleons.

311

312

313 The thresholds and trigger rates for each arm, as well as the coincidence rate (assuming  
 314 30ns coincidence window), are summarized in Table. I.

315

316 Note that for HCal, the “total rates” is either the sum of inclusive charged and neutral pions  
 317 evaluated with the Wiser cross sections *or* the “minimum bias” beam on target. We have  
 318 good reasons to think that the Wiser code results actually overestimate the HCal rates, but  
 319 for the sake of thoroughness, we have checked the coincidence rates assuming the sum of the  
 320 inclusive pions (evaluated with the Wiser cross sections) as the HCal rates.

321 In the worst case scenario, the coincidence rates could be as high as 5kHz, which might be  
 322 at the limit of manageability for the DAQ. However, a slight increase on the HCal threshold  
 323 (which would drop the efficiency from  $\sim 90\%$  to  $\sim 85\%$ ) would decrease the total HCal rates by  
 324  $\sim 35\%$  to  $40\%$  in this worst case scenario, which would make the situation more manageable  
 325 (3.3 kHz).

Point ( $\epsilon$ )	1 (0.599)		2 (0.838)	
	BigBite rates (Hz)	HCal rates (Hz)	BigBite rates (Hz)	HCal rates (Hz)
threshold (GeV)	1.32	0.106	2.99	0.090
Quasi-elastic	$1.62 \times 10^2$	$1.44 \times 10^2$	$4.39 \times 10^2$	$3.48 \times 10^2$
Inelastic	$1.62 \times 10^3$	-	$5.98 \times 10^3$	-
$\pi^-$ (Wiser)	$3.08 \times 10^2$	$1.40 \times 10^6$	$2.95 \times 10^2$	$1.96 \times 10^6$
$\pi^0$ (Wiser)	$1.15 \times 10^4$	$7.90 \times 10^6$	$1.69 \times 10^3$	$5.77 \times 10^6$
$\pi^+$ (Wiser)	$1.82 \times 10^2$	$2.87 \times 10^6$	$3.07 \times 10^2$	$3.34 \times 10^6$
Minimum bias	-	$3.39 \times 10^6$	-	$3.32 \times 10^6$ (*)
<i>Total</i>	$1.37 \times 10^4$	$1.22 \times 10^7$	$8.17 \times 10^3$	$1.11 \times 10^7$
(min. bias - HCal only)		/ $3.39 \times 10^6$		/ $3.32 \times 10^6$
<b>Coincidence rate</b>	$5.01 \times 10^3$		$2.72 \times 10^3$	
(with min. bias HCal)	$1.39 \times 10^3$		$8.14 \times 10^2$	

TABLE I. Trigger rates for BigBite and HCal, with the different process contributions separated, and the sum. For HCal, the total rates is either the sum of the (Wiser) inclusive pions or the minimum bias. The coincidence rates assume a 30 ns coincidence window.

326

## B. Contamination from inelastic

327

The main source of contamination for the quasi-elastic comes from the inelastic electron-nucleon scattering. Most of this contamination can be cleaned out thanks to a selection on the center of mass energy

$$W^2 = M_N^2 + 2M_N^2(E - E') - Q^2, \quad (8)$$

330 and the missing transverse momentum of the nucleon

$$p_{\perp miss} = \sqrt{(q_x - p'_x)^2 + (q_y - p'_y)^2}, \quad (9)$$

331 where  $M_N$  is the mass of the nucleon,  $E$  and  $E'$  the initial and final energy of the electron,  
332 and  $q_{x,y}$ ,  $p'_{x,y}$  are the projections on  $x$ ,  $y$  of the vectors of the virtual photon and final nucleon.

333 The distributions of these quantities (weighted with cross section and including detector res-  
 334 olutions) are displayed for quasi-elastic and inelastic scattering, and for proton and neutron,  
 335 on Fig. 10 for the low  $\epsilon$  kinematic, and on Fig. 11 for the high  $\epsilon$  kinematic. Provided that

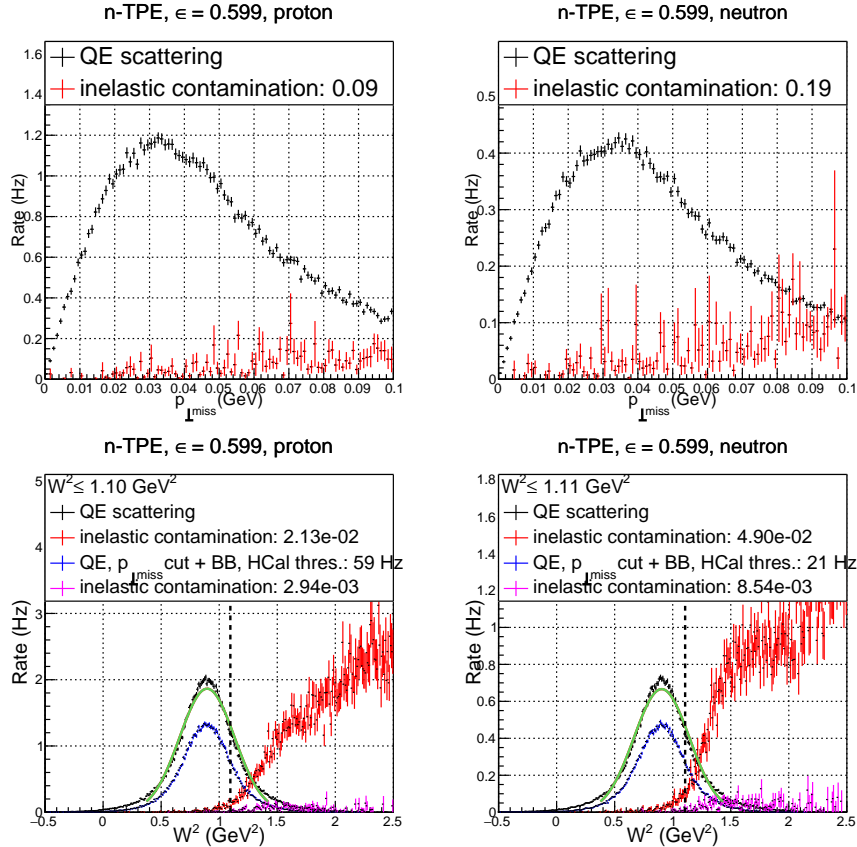


FIG. 10. Compared quasi-elastic and inelastic distributions (including detectors resolutions) for  $p_{\perp \text{miss}}$  (top) and  $W^2$  (bottom), for the low  $\epsilon$  kinematic. Comparison for protons is on the left, and comparison for neutrons is on the right. On the bottom panel, black and red are before the  $p_{\perp \text{miss}} \leq 0.1 \text{ GeV}$  selection, while blue and magenta are after  $p_{\perp \text{miss}} \leq 0.1 \text{ GeV}$  selection and application of BigBite shower and HCal thresholds.

336

338

339 we are not limited by statistics and the sample purity is capital for our experiment, we set  
 340 the selection criteria on  $W^2$  and  $p_{\perp \text{miss}}$  to maximize inelastic contamination (ideally below  
 341 1 %). Setting  $p_{\perp \text{miss}} \leq 0.1 \text{ GeV}$  and  $W^2 \leq 1.1 \text{ GeV}^2$ , the inelastic contamination of the

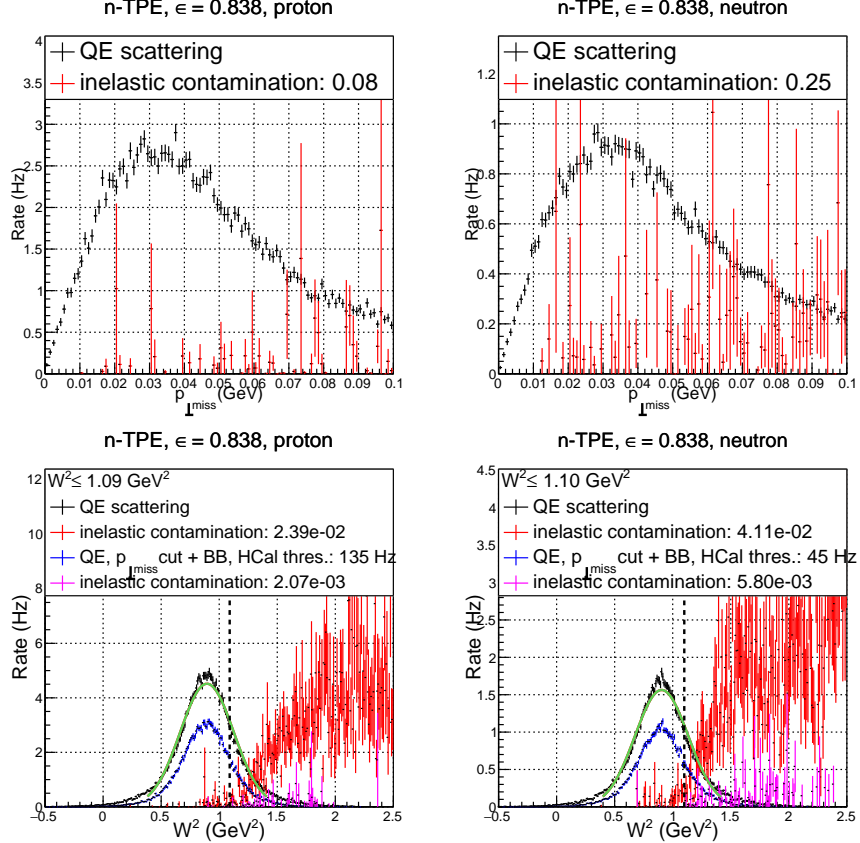


FIG. 11. Compared quasi-elastic and inelastic distributions (including detectors resolutions) for  $p_{\perp miss}$  (top) and  $W^2$  (bottom), for the high  $\epsilon$  kinematic. Comparison for protons is on the left, and comparison for neutrons is on the right. On the bottom panel, black and red are before the  $p_{\perp miss} \leq 0.1$  GeV selection, while blue and magenta are after  $p_{\perp miss} \leq 0.1$  GeV selection and application of BigBite shower and HCal thresholds.

342 elastic sample ranges from 0.2 % to 0.9 %, while retaining  $\geq 60$  % of the quasi-elastic events  
 343 properly recorded in the BigBite-SBS pair. Table. II summarizes the quasi-elastic selection  
 344 cuts, ad inelastic contamination  $\delta_{inel}$ .

Point ( $\epsilon$ )	$N$	$W^2$ cut	$p_{\perp miss}$ cut	$\delta_{inel}$
1 (0.599)	$n$	1.10	0.10	$2.94 \times 10^{-3}$
	$p$	1.11	0.10	$8.54 \times 10^{-3}$
2 (0.838)	$n$	1.09	0.10	$2.07 \times 10^{-3}$
	$p$	1.10	0.10	$5.80 \times 10^{-3}$

TABLE II. Summary of cuts for quasi-elastic selection and resulting inelastic contamination  $\delta_{inel}$ .

346

### C. Quasi-elastic counting rates

347 The signals for this experiment have been generated using the G4SBS elastic/quasi-elastic  
 348 generator. We generated a reasonably large sample of quasi-elastic events  $N_{Gen}$  for each  
 349 kinematics, on a solid angle  $\Delta\Omega_{Gen}$  that was larger than the detector acceptance. To evaluate  
 350 the detector solid angle, we define simple criteria that each event has to pass, defined as the  
 351 following;

- 352 • require a primary track, going through all 5 GEM layers (electron arm);
- 353 • require non-zero energy deposit in both the preshower and shower (electron arm);
- 354 • require non-zero energy deposit in HCal (hadron arm).

355 The detector solid angle, for both proton and neutron, are defined in Table. III. We also  
 356 define there the  $p$ - $n$  acceptance asymmetry  $A_{\Delta\Omega}$  such as

$$A_{\Delta\Omega} = \frac{(\Delta\Omega_e \otimes \Delta\Omega_n) - (\Delta\Omega_e \otimes \Delta\Omega_p)}{(\Delta\Omega_e \otimes \Delta\Omega_n) + (\Delta\Omega_e \otimes \Delta\Omega_p)} \quad (10)$$

357

358 Then, we evaluate the detection efficiency. For the electron, we require the energy recon-  
 359 structed in the BigBite calorimeter to be above a threshold defined as  $thr = \mu_E - 2.5 * \sigma_E$ ,  
 360 as well as a minimum number of GRINCH PMTs fired due to the primary electron; For  
 361 HCal, we require the threshold to be such as we obtain 90% efficiency. These values are  
 362 summarized in Table. IV. Quasi-elastic selection efficiency  $\eta_{sel}$  are also reminded.

Point ( $\epsilon$ )	$\Delta\Omega_e$ (msr)	$\Delta\Omega_e \otimes \Delta\Omega_n$ (msr)	$\Delta\Omega_e \otimes \Delta\Omega_p$ (msr)	$A_{\Delta\Omega}$ (%)
1 (0.599)	52.4	46.7	47.2	0.5
2 (0.838)	32.7	20.8	22.2	3.0

TABLE III. Kinematics electron solid angle, and convoluted electron/hadron solid angle, and acceptance asymmetry.

Point ( $\epsilon$ )	BB thr. (GeV)	HCal thr. (GeV)	$\eta_{det\ e}$	$\eta_{det\ n}$	$\eta_{det\ p}$	$\eta_{sel\ n}$	$\eta_{sel\ p}$
1 (0.599)	1.32	0.11	0.902	0.904	0.892	0.589	0.605
2 (0.838)	2.99	0.09	0.808	0.889	0.882	0.617	0.647

TABLE IV. Kinematics electron thresholds, particle detection efficiencies ( $\eta_{det}$ ), and efficiency of quasi-elastic selection  $\eta_{sel}$  separated for the proton and the neutron.

363

364        The counting rates are evaluated using among the  $N_{Gen}$  events generated the events that  
 365        have passed the selection described below, and weighting those events with the cross section  
 366         $d\sigma/d\Omega|_i$  calculated by G4SBS, multiplied by the generation solid angle  $\Delta\Omega_{Gen}$ , using the  
 367        formula:

$$N_{est} = \frac{\mathcal{L}_{exp}\Delta t}{N_{Gen}} \times \sum_{i \in \text{accepted evts}} \left( \frac{d\sigma}{d\Omega} \Big|_i \times \Delta\Omega_{Gen} \right) \quad (11)$$

368        with  $\mathcal{L}_{exp}$  the experimental luminosity and  $\Delta t$  the running time Events are “accepted” if  
 369        they meet the following criteria:

- 370        • the electron is in the BigBite acceptance;
- 371        • the electron passes the BigBite threshold defined in Table IV and gives signal in the  
 372        GRINCH;
- 373        • the nucleon is in the HCal acceptance and passes the HCal threshold defined in Ta-  
 374        ble IV;

- 375     • the event passes the quasi-elastic selection defined in the previous section *i.e.*  $W^2 \leq 1.1 \text{ GeV}^2$   
 376     and  $p_{\perp miss} \leq 0.10 \text{ GeV}$ .

377     The total quasi-elastic statistics  $N_{QE}$ , as well as the total form factor:  $F^2$

$$F^2 = \frac{N_{QE}}{\mathcal{L}_{exp} \cdot \Delta t \cdot d\sigma_{Mott}/d\Omega \cdot \Delta\Omega \cdot \eta} \quad (12)$$

378     and its statistical error  $\Delta F^2 = F^2 / \sqrt{N_{QE}}$  are compiled for both kinematics in Table. V,  
 379     assuming a running time  $\Delta t = 12$  hours of running at a beam intensity of  $I_{exp} = 30 \mu\text{A}$  on  
 380     a liquid deuterium target with length  $l_{tgt} = 15 \text{ cm}$  and density  $d_{tgt} = 0.169 \text{ g.cm}^{-3}$ .

Point ( $\epsilon$ )	$N_{QE}$ (e-n)	$N_{QE}$ (e-p)	$F_n^2$ ( $\times 10^{-3}$ )	$\Delta F_n^2$ ( $\times 10^{-6}$ )	$F_p^2$ ( $\times 10^{-3}$ )	$\Delta F_p^2$ ( $\times 10^{-6}$ )
1 (0.599)	$9.07 \times 10^5$	$2.55 \times 10^6$	0.99	1.04	2.73	1.70
2 (0.838)	$1.94 \times 10^6$	$5.83 \times 10^6$	0.72	0.52	1.93	0.80

TABLE V. Quasi-elastic counting rates, and total form factor (defined in Eq. 11). These rates assume  $\Delta t = 12$  hours of running at a beam intensity of  $I_{exp} = 30 \mu\text{A}$  on a liquid deuterium target with length  $l_{tgt} = 15 \text{ cm}$  and density  $d_{tgt} = 0.169 \text{ g.cm}^{-3}$

381

382     The expression of the total form factor  $F^2$  is: where  $\Delta t$  the running time,  $\Delta\Omega$  is the  
 383     convoluted BigBite-HCal solid angle,  $\eta$  is the product of all efficiencies (detection efficiencies  
 384      $\eta_{det} \times$  selection efficiency  $\eta_{sel}$ ), and  $\mathcal{L}_{exp}$  is the experimental luminosity:

$$\mathcal{L}_{exp} = \frac{I_{exp}}{q_e} * L_{tgt} * d_{tgt} \frac{\mathcal{N}_A}{m_D}. \quad (13)$$

385     The calculation of the  $F_2$  term requires the evaluation of the Mott cross section

$$\frac{d\sigma_{Mott}}{d\Omega} = (\hbar c \alpha_{EM})^2 \left( \frac{e}{2E} \right)^2 \left( \frac{\cos\theta_e/2}{\sin^2\theta_e/2} \right)^2 \frac{E'}{E} \quad (14)$$

386     The Mott cross section has been calculated with the weighted average of the electron variables  
 387     (momentum and polar angle).

388

Point ( $\epsilon$ )	$\langle \theta_e \rangle$ (deg)	$\langle k' \rangle$ (GeV)	$\langle Q^2 \rangle$ (GeV $^2$ )	$\sigma_{Mott}$ (nb sr $^{-1}$ )
1 (0.599)	41.7	2.01	4.47	6.62
2 (0.838)	22.9	4.26	4.40	48.0

TABLE VI. Cross-section weighted average of kinematic variables over the BigBite acceptance.

The Mott cross section has been evaluated at these values.

389

## VI. SYSTEMATIC ERRORS

390 In this section we will estimate (or set upper limits on) the contributions to the systematic  
 391 uncertainty for this experiment. The sources of systematic uncertainties from the experi-  
 392 mental setup (target, acceptance, inelastic contamination) were already estimated for the  
 393 SBS  $G_M^n$  experiment proposal [19]. Note that some of those systematics (nuclear corrections,  
 394 accidentals) cancel in the ratio  $R = f_{corr} \times N_{e,e'n}/N_{e,e'p}$ . Since the experimental setup has  
 395 evolved since then, some of these uncertainties have been reevaluated, namely the acceptance  
 396 loss and inelastic contamination.

TABLE VII. Estimated contributions (in percent) to systematic errors on TPE. Quantities marked with \* are taken from the SBS  $G_M^n$  experiment proposal [19].

Kinematic ( $\epsilon$ )	(1) 0.599	(2) 0.838
Nuclear correction*	-	
Accidentals*	-	
Target windows*	0.2 %	
Acceptance losses	0.5 %	3.0 %
Inelastic contamination	0.9 %	0.6 %
Nucleon mis-identification*	0.6 %	
Syst. error on $R = f_{corr} \times N_{e,e'n}/N_{e,e'p}$	1.3 %	3.1 %
$S_c^n = \sigma_L^n/\sigma_T^n$	$0.107 \pm 0.01$ (9.3 %)	
$\mu_n G_E^n/G_M^n$	$0.55 \pm 0.05$ (9.1 %)	
Syst. error on TPE	$0.069 \pm 0.012$ (17.4 %)	

397 Table. VII lists the estimated contributions to systematic errors on the two-photon-  
 398 exchange contribution (TPE). The systematics for  $S_c^n$  and  $\mu_n G_E^n/G_M^n$  have already been ex-  
 399 plied in Sec. III, and are the leading contributions to the total uncertainty.

400 Inelastic contamination has been reevaluated in Sec. V B. To evaluate the upper limit on

<sup>401</sup> our uncertainty, we added quadratically the inelastic contamination evaluated for the proton  
<sup>402</sup> and the neutron for each kinematics, which is the error we make if we ignore the systematics  
<sup>403</sup> completely. Even in this case, we expect less than 1% systematic errors.

<sup>404</sup> The acceptance loss in SBS (*i.e.* the proportion of non-detected nucleons for each detected  
<sup>405</sup> electron) have been evaluated for both kinematics. They are about 10% for the  $\epsilon = 0.60$   
<sup>406</sup> kinematic (meaning that for every good electron measured, we will not measure the recoil  
<sup>407</sup> nucleon 10% of the times), but they are over 30 % for the  $\epsilon = 0.84$  kinematics, which is due to  
<sup>408</sup> a larger spread of the nucleon imprint. The systematic uncertainty on the acceptance loss for  
<sup>409</sup> the ratio  $R = f_{corr} \times N_{e,e'n}/N_{e,e'p}$  is maximized by the proton-neutron solid angle asymmetry  
<sup>410</sup>  $A_{\Delta\Omega} = \Delta\Omega_n - \Delta\Omega_p/\Delta\Omega_n + \Delta\Omega_p$ . This asymmetry is about 0.5% for the  $\epsilon = 0.60$  kinematic  
<sup>411</sup> (consistent with the  $G_M^n$  proposal), but goes up to 3% for the  $\epsilon = 0.84$  kinematics.

412

## VII. PROPOSED MEASUREMENTS

413 We propose to use the same experimental setup of E12-09-019 experiment. We will add  
 414 a kinematic point at  $Q^2 = 4.5 \text{ (GeV/c)}^2$ , but with a higher  $\epsilon$  value. This additional point  
 415 along with the data point of E12-09-019 experiment will allow us to perform LT separation  
 416 and obtain (in one-photon approximation) the  $G_E^n$  value. Table. VIII displays the kinematic  
 417 setting of the proposed experiment.

Point	$Q^2$ (GeV/c) $^2$	E (GeV)	E' (GeV)	$\theta_{BB}$ degrees	$\theta_{SBS}$ degrees	$\epsilon$	$\Delta\sigma$ (%)	$\Delta TPE$ (%)
1	4.5	4.4	2.0	41.88	24.67	0.599		
2	4.5	6.6	4.2	23.23	31.2	0.838		

TABLE VIII. Kinematic settings of the proposed experiment. The blue row is a kinematic point of E12-09-019 experiment.

418

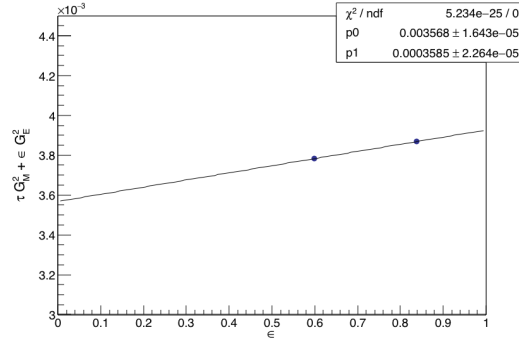


FIG. 12. The reduced cross section (model) as a function of  $\epsilon$

419 The reduced cross section

$$\sigma_R = \epsilon G_E^2 + \tau G_E^2 \quad (15)$$

<sup>420</sup> is displayed as a function of  $\epsilon$  on Fig. 12. Admitting the prediction from [4], the neutron two-  
<sup>421</sup> photon exchange contribution would amount to  $0.069 \pm 0.010(stat.) \pm 0.012(syst.)$ , which  
<sup>422</sup> would be a  $\geq 4\sigma$  observation of this quantity.

423

### VIII. BEAM TIME REQUEST

424     **We request 48 hours total time (32 hours of beam-on target)** to measure the  
 425     two-photon effect (and  $G_E^n$  in one-photon approximation) at  $Q^2 = 4.5$  ( $\text{GeV}/c$ )<sup>2</sup> through a  
 426     measurement of the cross sections of the reaction  $D(e,e'N)$  at a large value of the virtual  
 427     photon polarization  $\epsilon=0.84$ . *The measurement at  $Q^2 = 4.5$  ( $\text{GeV}/c$ )<sup>2</sup>,  $\epsilon=0.60$  is already*  
 428     *scheduled as part of the SBS  $G_M^n$  experiment E12-09-019 [19].*

429     We plan to take 12 hours of data at a full luminosity of  $2.86 \times 10^{38} \text{ cm}^{-2}\text{s}^{-1}$ , which  
 430     corresponds to a beam intensity of  $I_{exp} = 30 \mu\text{A}$  on a liquid deuterium target with length  
 431      $l_{tgt} = 15 \text{ cm}$  and density  $d_{tgt} = 0.169 \text{ g.cm}^{-3}$ . To have a better handle on our backgrounds,  
 432     we also plan to take 12 hours of data at half luminosity (basically by lowering the beam  
 433     intensity by a factor 2). In each of these configurations, we also need to take data on a  
 434     “dummy” target (*i.e.* on a target cell identical to the one used for production, but empty)  
 435     to understand the contamination of our data from the target walls.

436     In addition to this beam time, we also require 16 hours (two shifts) to change the exper-  
 437     imental configuration. This configuration change means:

- 438       • SBS magnet and the hadronic calorimeter (HCal) angle change;
- 439       • BigBite spectrometer angle and distance change;
- 440       • Beam energy change;

441     These tasks may be done in parallel, but the SBS configuration is the most-time consuming  
 442     task, and determines the time required to perfomr this configuration change.

443     The projected use of this time is summarized in Table. IX.

444

445     This experiment will take place in Hall A, along the already scheduled SBS  $G_M^n$  experiment  
 446     E12-09-019, utilizing the BigBite spectrometer to detect electrons scattered off the liquid  
 447     deuterium target, and HCal calorimeter to detect the recoiling neutron and proton.

Task	Target	$I_{exp}$	time requested
Data taking (Prod.)	15 cm LD <sub>2</sub>	30 $\mu$ A	12 hours
Data taking (Syst.)	15 cm “Dummy”	30 $\mu$ A	4 hours
Data taking (Prod.)	15 cm LD <sub>2</sub>	15 $\mu$ A	12 hours
Data taking (Syst.)	15 cm “Dummy”	15 $\mu$ A	4 hours
Setting changes (SBS, BigBite angles, beam energy)			16 hours
<b>Total</b>			<b>48 hours</b>

TABLE IX. Summary table for the beam time request. Setting changes include SBS and Bigte bite angles change, as well as a beam energy change.

448 Data taking (if approved by PAC48) will take place in summer 2021 during the approved  
 449 and scheduled run of the GMn, E12-09-019, experiment, which is going to measure the  $e - n$   
 450 elastic scattering cross section at  $Q^2 = 4.5$  (GeV/c)<sup>2</sup> at  $\epsilon=0.60$ .

451 The set of instrumentation and required beam current for proposed measurement is iden-  
 452 tical to one in the GMn experiment. The beam energy of 6.6 GeV will be used. One of two  
 453 data points required for the cross section LT separation is already in the data taking plan of  
 454 GMn.

455 There are no other measurements of TPE in the  $e - n$  elastic scattering and knowledge  
 456 of the TPE is essential for the understanding of the elastic electron scattering from neutron  
 457 (and proton) and hadron structure. Furthermore, it is a necessary input in the analysis and  
 458 interpretation of a wide range of electron scattering processes.

459 The kinematics of our measurements emphasize the same  $Q^2$  range where TPE in  $e - p$   
 460 elastic scattering was observed to dominate in Rosenbluth slope. Measuring at this high  
 461 momentum transfers will provide unique input for testing TPE calculations [4].

462 We propose to measure the Rosenbluth slope and extract (in one-photon approximation)  
 463  $\delta G_E^n/G_M^n$  to an accuracy of 0.15, which would bring its precision to a level comparable with  
 464 that of the double polarization experiments GEN-RP and GEN-He3 at such value of  $Q^2$ .  
 465 Such precision should be sufficient to detect the TPE contribution to the  $e - n$  Rosenbluth  
 466 slope on the three sigma level.

- 
- 467 [1] R. Hofstadter, *Rev. Mod. Phys.* **28**, 214 (1956).
- 468 [2] M. N. Rosenbluth, *Phys. Rev.* **79**, 615 (1950).
- 469 [3] E. Christy *et al.*, “Two-photon exchange in electron-proton elastic scattering at large four-  
470 momentum transfer,” (2020), in preparation for publication in PRL.
- 471 [4] P. G. Blunden, W. Melnitchouk, and J. A. Tjon, *Phys. Rev.* **C72**, 034612 (2005), arXiv:nucl-  
472 th/0506039 [nucl-th].
- 473 [5] J. Arrington, P. G. Blunden, and W. Melnitchouk, *Prog. Part. Nucl. Phys.* **66**, 782 (2011),  
474 arXiv:1105.0951 [nucl-th].
- 475 [6] A. Afanasev, P. Blunden, D. Hasell, and B. Raue, *Prog. Part. Nucl. Phys.* **95**, 245 (2017),  
476 arXiv:1703.03874 [nucl-ex].
- 477 [7] B. Wojtsekhowski, in *Exclusive processes at high momentum transfer. Proceedings, Newport  
478 News, USA, May 15-18, 2002* (2002) arXiv:1706.02747 [physics.ins-det].
- 479 [8] G. D. Cates, C. W. de Jager, S. Riordan, and B. Wojtsekhowski, *Phys. Rev. Lett.* **106**, 252003  
480 (2011), arXiv:1103.1808 [nucl-ex].
- 481 [9] C. D. Roberts, M. S. Bhagwat, A. Holl, and S. V. Wright, *Eur. Phys. J. ST* **140**, 53 (2007),  
482 arXiv:0802.0217 [nucl-th].
- 483 [10] J. Segovia, I. C. Cloet, C. D. Roberts, and S. M. Schmidt, *Few Body Syst.* **55**, 1185 (2014),  
484 arXiv:1408.2919 [nucl-th].
- 485 [11] B. Wojtsekhowski (2020) arXiv:2001.02190 [nucl-ex].
- 486 [12] G. A. Miller, *Phys. Rev. Lett.* **99**, 112001 (2007), arXiv:0705.2409 [nucl-th].
- 487 [13] C. E. Carlson and M. Vanderhaeghen, *Phys. Rev. Lett.* **100**, 032004 (2008), arXiv:0710.0835  
488 [hep-ph].
- 489 [14] D. Muller, D. Robaschik, B. Geyer, F. M. Dittes, and J. Horejsi, *Fortsch. Phys.* **42**, 101  
490 (1994), arXiv:hep-ph/9812448 [hep-ph].
- 491 [15] X.-D. Ji, *Phys. Rev. Lett.* **78**, 610 (1997), arXiv:hep-ph/9603249 [hep-ph].
- 492 [16] A. V. Radyushkin, *Phys. Lett.* **B380**, 417 (1996), arXiv:hep-ph/9604317 [hep-ph].

- 493 [17] M. Diehl and P. Kroll, *Eur. Phys. J.* **C73**, 2397 (2013), arXiv:1302.4604 [hep-ph].
- 494 [18] N. Kivel, “private communications,” (2020).
- 495 [19] J. Annand, R. Gilman, B. Quinn, B. Wojtsekhowski, *et al.*, unpublished. See [https://www.jlab.org/exp\\_prog/proposals/09/PR12-09-019.pdf](https://www.jlab.org/exp_prog/proposals/09/PR12-09-019.pdf), [https://www.jlab.org/exp\\_prog/proposals/proposal\\_updates/PR12-09-019\\_pac35.pdf](https://www.jlab.org/exp_prog/proposals/proposal_updates/PR12-09-019_pac35.pdf) (2008).
- 496 [20] E. B. Hughes, T. A. Griffy, M. R. Yearian, and R. Hofstadter, *Phys. Rev.* **139**, B458 (1965).
- 497 [21] R. G. Arnold *et al.*, *Phys. Rev. Lett.* **61**, 806 (1988).
- 498 [22] L. Durand, *Phys. Rev.* **115**, 1020 (1959).
- 499 [23] E. E. W. Bruins *et al.*, *Phys. Rev. Lett.* **75**, 21 (1995).
- 500 [24] G. Kubon *et al.*, *Phys. Lett.* **B524**, 26 (2002), arXiv:nucl-ex/0107016 [nucl-ex].
- 501 [25] J. Lachniet *et al.* (CLAS), *Phys. Rev. Lett.* **102**, 192001 (2009), arXiv:0811.1716 [nucl-ex].
- 502 [26] V. Punjabi, C. F. Perdrisat, M. K. Jones, E. J. Brash, and C. E. Carlson, *Eur. Phys. J.* **A51**, 79 (2015), arXiv:1503.01452 [nucl-ex].
- 503 [27] A. Puckett, unpublished. See [https://hallaweb.jlab.org/wiki/index.php/Documentation\\_of\\_g4sbs](https://hallaweb.jlab.org/wiki/index.php/Documentation_of_g4sbs) (2016).
- 504 [28] D. E. Wiser, “Photoproduction of protons, kaons and pions at slac energies,” Ph.D. thesis,
- 505 University of Wisconsin (1977).